Three-Axis Capacitive Sensor Arrays for Local and Global Shear Force Detection

Jayer Fernandes, *Student Member, IEEE*, Jiangang Chen, and Hongrui Jiang, *Fellow, IEEE*

Abstract—We report the real time characterization and measurement results of a new tri-axial capacitive sensing array. Each unit cell of the Kapton based sensor has an overlapping electrode geometry that allows for the measurement of normal and shear force magnitudes, and the estimation of the 2D and 3D angle of the shear force. The use of a patterned Ecoflex dielectric layer further improves the shear force response and the tunability of the sensor. A custom readout circuit was developed to selectively read the differential capacitances in the sensor array. The local (unit cell) and global (array) force response of the sensor was characterized using a tilt stage, allowing us to determine both the normal and the shear response at different angles in the range of 0-20N. The results show that the Unit Cell response is uniform in the linear range of 0-10N for normal forces (4.6fF/N for all four differential capacitances) and shows good sensitivity for shear forces (1.4 fF/N difference between the right and left differential capacitances at the minimum) and low cross talk. Similar results were seen when a global force was applied across the sensor array. 2D and 3D models were developed to extrapolate the shear force angle from the capacitance data. We also characterized the flexible patterned dielectric layer to understand the effect of its structural dimensions on the effective relative permittivity and developed an analytical model to easily calculate the effective relative permittivity, which showed excellent correlation with the experimentally obtained results.   [2020-0382]

Index Terms—Flexible electronics, capacitive sensing, tactile sensing, shear force, normal force, dielectric, soft lithography, three-axis capacitive sensor.

I. INTRODUCTION

SHEAR forces, along with normal forces, play an important role in the world around us. They are essential as a feedback mechanism in tactile sensing, which in turn finds wide applications in manufacturing [1], healthcare [2] and robotics [3]. In the realm of biomechanics, shear forces are implicit in everyday biomechanical tasks such as object gripping and manipulation [4], and in activities related to gait biomechanics

such as walking and running and even conditions such as pressure ulcers [5]–[8]. Consequently, imbalances in shear forces have significant medical implications and are common to a large number of medical conditions that impair the motor system such as Parkinson's Disease, lower limb injuries or amputations and muscular atrophy, where they can manifest as gait imbalances, gait shuffling and ultimately falls [9]–[13].

Commerically available methods of measuring biomechechanical parameters related to gait and grip generally fall into the categories of optical systems, gait walkways, piezoelectric pressure mats, multi-axis force sensors and inertial measurement units (IMUs) [14]–[16]. These systems are prohibitively expensive, limiting their use to research and clinical settings. This makes it difficult to monitor individuals remotely as they perform their activities of daily living and instead, forces the determination of biomechanical parameters using a prescribed set of manouevers/actions. It is a known fact that clinical/laboratory environments can cause bias in measurements by introducing deviations in walking and gripping patterns, as well as through the introduction of potential patient-doctor expectancy effects [17], [18]. Additionally, clinical evaluations offer only limited temporal snapshots of the dynamic changes that occur [19]. A significant drawback of these systems is that they are incapable of measuring changes in shear forces or giving any sort of qualitative information about the direction or angle of the shear force at the respective interface [20]–[23].

There have been several approaches to the design of sensors for the measurement of normal and shear forces. MEMS processing techniques have been extensively deployed for the fabrication of triaxial capacitive sensors in the past [24]–[27]. The utilization of MEMS fabrication technology allows for the development of precision sensors with high spatial resolutions and sensitivities. Additionally, tactile sensors built on flexible substrates such as polyimide offer a solution to the issue of stiffness/rigidity [28]. However, these sensors rely on standard silicon fabrication techniques, with a large number of intermediate cleanroom processing steps, which prevents the rapid prototyping of devices.

More recently, there has been a lot of interest in the development of flexible/compliant force sensors that are based on elastomeric materials such as Ecoflex and polydimethylsiloxane (PDMS) [29]–[31]. The stretchable nature of these materials allows for the realization of conformal and compliant wearable sensors, where the elastomers either comprise the sensor encapsulation [32] or are used as a layer in the sensor structure that responds to normal and shear forces such as those used in the actuation of optical shear force

sensors [33] and the dielectric layer in capacitive shear force sensors [31], [32]. The use of metals with elastomers for the purpose of electrical contact generally poses a number of fabrication challenges. They often demonstrate poor adhesion to the elastomer and require the use of an intermediate adhesion layer such as Parylene-C. These adhesion layers have different material properties such as thermal coefficient of expansion, stiffness and strain coefficients compared to the elastomer, which affects the device operating range and complicates the fabrication process by limiting the temperature ranges that can be used. The cracking of the electrodes due to the mismatch in the properties of the adhesion and elastomeric layers is a very common problem. Workarounds to this generally involve building the electrodes into the elastomer layer through the use of liquid metals [36] or by reducing the resistance of the elastomer by using conductive filler materials such as carbon black and silver nanoparticles, in order to build conductive elastomeric pathways that are mechanically compliant [37]. In all of these cases, the use of a solid elastomer film layer significantly limits the ability of the sensor to respond to shear forces effectively and the shear force sensing range. In addition, the fabrication process for these sensors is complex and expensive, limiting the ability to rapidly prototype devices with different properties, based on the applications need.

Our previous work reported the development of a low-cost, flexible and robust three-axis capacitive touch-force sensor single unit cell structure that was capable of discerning both normal and shear forces and could provide some limited qualitative information about the direction of the force [38]. In this paper, we report the development of a multiplexed array of these tri-axial unit cells, with the goal of obtaining information about the normal and shear force components both at the local (unit cell) level and global (array) level. We look into the extrapolation of the shear force angle from the differential capacitance data presented by each unit cell. As shown previously in [35], it is possible to manually discern the general direction of the shear force by observing the trend in the four differential capacitance signals in the unit cell and thresholding the signals to examine their relative peaks. This approach becomes cumbersome when extended to an array and necessitates the development of models to ascertain the angle from the capacitance data. The sensor was also further characterized under cyclic and static loading conditions to test the robustness of the sensor and the repeatability of the results under different kinds of shear loads. This work also aims to quantify some of the properties of the dielectric layer, which is an essential aspect to the sensor characterization.

II. SENSOR DESIGN

A. Sensing Method

The operating principle of the sensor is based on the change in the differential capacitances between the central top electrode and the four bottom electrodes in a unit cell structure, in response to either a normal or a shear force. A normal force compresses the dielectric layer, which reduces the distance between the plates of the capacitor and increases the capacitances of all four differential capacitors in the
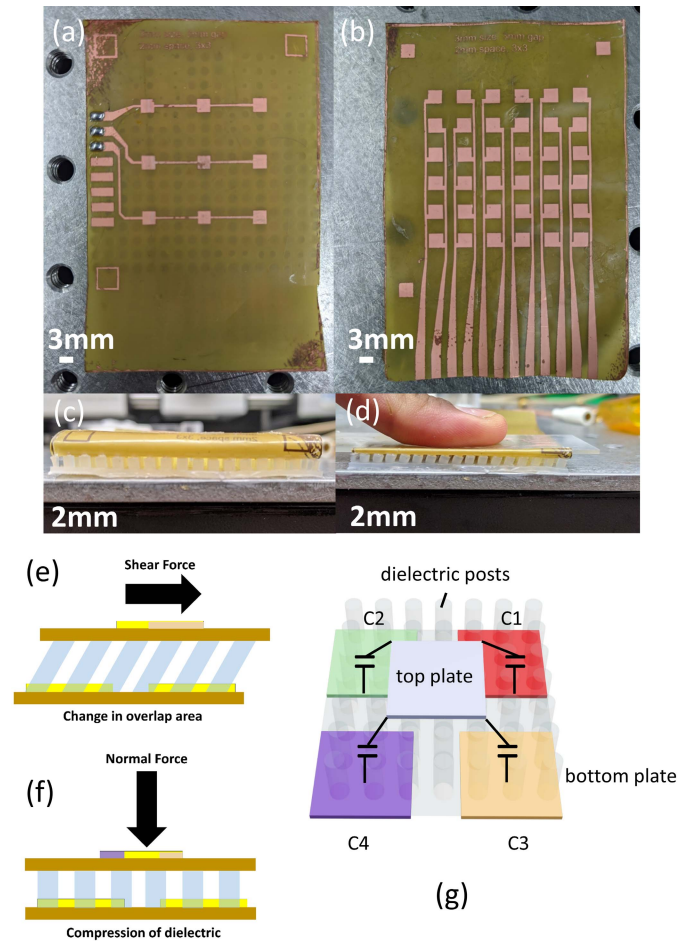

Fig. 1. Device image of a 3 × 3 multiplexed sensor array. Each plate has a side of 3mm, and the spacing between the bottom electrode plates is 2mm. (a) Image of fabricated top electrode array. (b) Image of fabricated bottom electrode array. (c) Image of the patterned dielectric layer. (d) The effect of a shear force load on the dielectric layer posts. (e) Schematic showing the behavior of the dielectric layer under a shear force. The orange in the top electrode indicates the overlap area between the top and bottom electrodes. (f) Schematic showing the behavior of the dielectric layer under a normal force. The orange and purple in the top electrode indicates the overlap area between the top and bottom electrodes. (g) Unit cell schematic showing the overlapping geometry and patterned dielectric layer.

sensor unit cell uniformly. The application of a tangential/shear force results in the lateral movement of the top plate with respect to the bottom plates, increasing the overlap area, and consequently the differential capacitances in that direction.

B. Sensor Structure

As shown in Fig. 1, the array structure comprises of a top and bottom Kapton layer, which make up the top and bottom electrode structures of the array, respectively, and a flexible patterned layer of Ecoflex-30 between the electrodes, which serves as the dielectric layer. Within the array, each sensing unit cell is multiplexed to allow for the sequential polling of the four individual differential capacitors, with the top plates being row multiplexed and the bottom plates being read in a column multiplexed fashion. A schematic of the unit cell is shown in Fig. 1 (e). The non-symmetric top and bottom electrode structures necessitate the use a different number
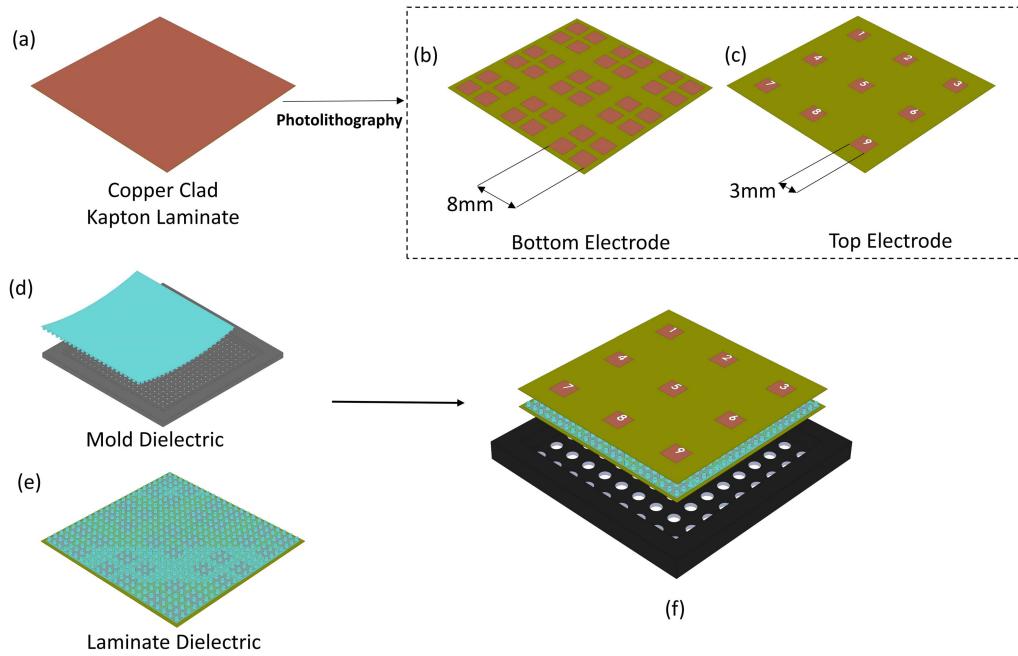
Fig. 2. Shows a schematic of the fabrication of the sensor array. (a) The starting copper clad Kapton laminate. Photolithography and copper etchant are used to define the (b) bottom electrodes and (c) top electrodes. (d) The dielectric layer is fabricated using a 3D printed mold and (e) laminated to the bottom electrode layer. (f) Finally, the top and bottom layers are aligned using alignment marks and a jig and cured together on a hot plate to fabricate the array.

of readout channels for the top electrodes and the bottom electrodes. In the case of the 3×3 array, it would require three readout lines for the top electrodes and twelve readout lines for the bottom electrodes.

III. SENSOR FABRICATION

The fabrication of the sensor relies on the use of rapid prototyping and soft lithography techniques. The electrode layers were fabricated from sheets of Dupont Pyralux AC0092500EV copper clad Kapton laminates that were cut to a size of $3'' \times 2''$ and thoroughly cleaned with acetone and isopropyl alcohol (IPA) to remove oils and other surface residues. Photolithography was performed to define the top and bottom electrodes separately. APS-100 Copper Etchant (Transene Company, Inc.) was used to etch the copper from the Kapton laminate to form the top and bottom electrodes. In the meanwhile, Ecoflex-30 silicone was poured into a 3D printed mold patterned with holes, degassed in a vacuum chamber to remove air bubbles and allowed to partially cure before transferring the bottom Kapton layer on top of it, bonding it and allowing both parts to cure as a uniform piece at 75°C on a hotplate for 4 hours. The back of the top electrode Kapton sheet was coated with a small amount of Ecoflex-30 to facilitate its bonding to the dielectric layer. The top and bottom electrode layers are aligned using a 3D printed jig and alignment marks as shown in Fig. 2, to ensure good centering of the top electrode over the four bottom electrodes.

IV. ANGLE ESTIMATION TECHNIQUES

A. Two Dimensional Case

Fig. 3 shows a simplified schematic of the sensor under an in-plane shear force F. In the initial configuration, the top electrode is centered over the bottom electrodes and has an overlap area A_1 with sides x_1 and y_1. In an ideal situation where there are no fabrication errors, the top plate is centrally aligned with respect to the bottom plates, implying that all the overlap areas are equal and hence, $x_1 = y_1 = a$. A shear force F, applied in a given direction, increases the overlap area in that direction to a new value A_2 with dimensions x_2 and y_2.

The primary assumption in the two-dimensional case is that the top plate in the sensor unit cell moves parallel to the bottom plate, without any significant change in the gap between them.

The initial capacitance of C_1 is given by

$$C_1 = \frac{\epsilon_o \epsilon_r A_1}{d} = \frac{\epsilon_o \epsilon_r x_1 y_1}{d} \tag{1}$$

where ϵ_o and ϵ_r are the free-space and dielectric layer effective permittivities, respectively, and d is the distance between the capacitor plates.

Since the shear force changes the overlap area from A_1 to A_2, the new capacitance for C_1 is

$$C_{1new} = \frac{\epsilon_o \epsilon_r A_2}{d} = \frac{\epsilon_o \epsilon_r x_2 y_2}{d} = \frac{\epsilon_o \epsilon_r (x_1 + \delta_x)(y_1 + \delta_y)}{d} \tag{2}$$

The change in capacitance for the first differential capacitor is given by

$$\Delta C_1 = C_{1new} - C_1 = \frac{\epsilon_o \epsilon_r (x_1 \delta_y + y_1 \delta_x + \delta_x \delta_y)}{d} \tag{3}$$

Since, x_1 and y_1 are equal, the above equation becomes

$$\Delta C_1 = \frac{\epsilon_o \epsilon_r a}{d} \left(\delta_x + \delta_y + \frac{\delta_x \delta_y}{a} \right) \tag{4}$$
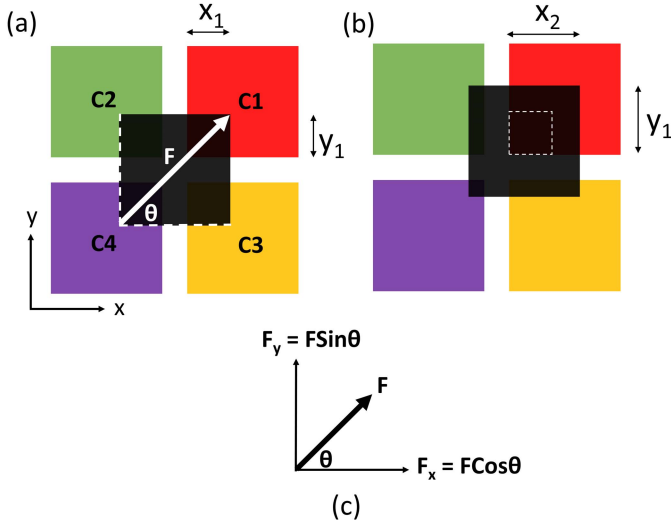
Fig. 3. (a) Schematic of the sensor unit cell in its initial configuration with an in-plane shear force F applied to the top plate. (b) Schematic of the sensor unit cell after the force is applied, indicating the displacement of the top plate with respect to the bottom electrodes. The original overlap area between the top electrode and one of the bottom electrodes is indicated by the white dashed box. At bottom is the resolution of the shear force into its x and y components. (c) Resolution of the of the shear force F into its respective two dimensional components.
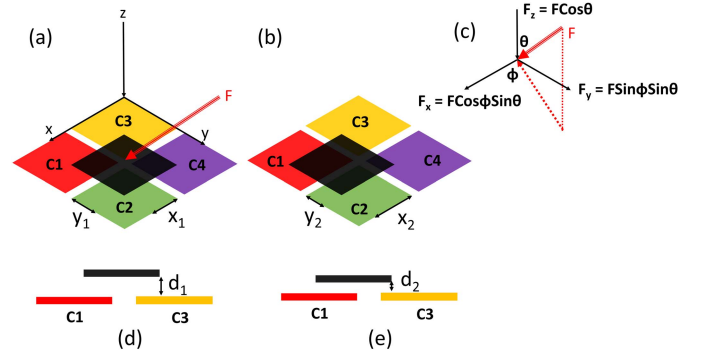

Fig. 4. (a) Schematic of the sensor unit cell in the three dimensional space in its initial configuration with a shear force F applied to the top plate. (b) Schematic of the sensor unit cell after the force is applied, indicating the displacement of the top plate with respect to the bottom electrodes and the change in the overlap area. (c) Resolution of the shear force F into its respective components. (d) Side view of the unit cell in its original configuration, showing the distance between the top and bottom electrodes (e) Side view of the unit cell after the application of the shear force F, showing the displacements of the electrodes and the compression of the dielectric layer.

The changes in capacitance for the remaining three differential capacitors are

$$\Delta C_2 = \frac{\epsilon_0 \epsilon_r a}{d} \left(-\delta_x + \delta_y - \frac{\delta_x \delta_y}{a} \right) \quad (5)$$

$$\Delta C_3 = \frac{\epsilon_0 \epsilon_r a}{d} \left(\delta_x - \delta_y - \frac{\delta_x \delta_y}{a} \right) \quad (6)$$

$$\Delta C_4 = \frac{\epsilon_0 \epsilon_r a}{d} \left(-\delta_x - \delta_y + \frac{\delta_x \delta_y}{a} \right) \quad (7)$$

The in-plane force F can be resolved into its individual components, which in turn, is written in terms of the displacements using Hooke's Law, in the linear regime.

$$F_x = F \cos(\theta) = k\delta_x \quad (8)$$

$$F_y = F \sin(\theta) = k\delta_y \quad (9)$$

where k is the spring constant of the dielectric layer.

Combining the above set of equations, we obtain

$$\cos(\theta) = \frac{kd\,(\Delta C_1 + \Delta C_3)}{2\epsilon_0 \epsilon_r aF} = \frac{kd\,(\Delta C_2 + \Delta C_4)}{2\epsilon_0 \epsilon_r aF} \quad (10)$$

$$\sin(\theta) = \frac{kd\,(\Delta C_1 + \Delta C_2)}{2\epsilon_0 \epsilon_r aF} = \frac{kd\,(\Delta C_3 + \Delta C_4)}{2\epsilon_0 \epsilon_r aF} \quad (11)$$

The shear force angle in two dimensions can be obtained from the above equations as

$$\theta = \tan^{-1}\left(\frac{\Delta C_1 + \Delta C_2}{\Delta C_1 + \Delta C_3} \right) = \tan^{-1}\left(\frac{\Delta C_4 + \Delta C_3}{\Delta C_4 + \Delta C_2} \right) \quad (12)$$

In the two-dimensional case, the direction of the shear force can be easily determined using just three differential capacitances.

The first equation covers cases involving C_1, C_2 and C_3, i.e., angles between 270 degrees and 180 degrees in the anticlockwise direction. The second equation involves C_2, C_3

and C_4, covering angles between 90 degrees and 360 degrees in the anticlockwise direction. For example, an upward directed shear force results in equal positive changes in C_1 and C_2, and an equal negative change in C_3, resulting in a θ value of 90 degrees.

The relationship between the components of the applied force and the change in capacitance can be derived as

$$F_x = \frac{ka(\Delta C_1 + \Delta C_3)}{2C_1} = \frac{-ka(\Delta C_2 + \Delta C_4)}{2C_1} \quad (13)$$

$$F_y = \frac{ka(\Delta C_1 + \Delta C_2)}{2C_1} = \frac{-ka(\Delta C_3 + \Delta C_4)}{2C_1} \quad (14)$$

B. Three Dimensional Case

The determination of the three dimensional shear force angle, along with the direction of the shear force has many significant applications in the biomedical realm, such as determining the angle of the forces at the feet in the events leading up to a fall and at the fingertips, when the grip on an object is lost and the object slips.

In the previous section (simplified case of the detection of an in-plane shear force direction in the two dimensional space), the primary assumption was that the top electrode of the unit cell moves parallel to the bottom electrodes, without compressing the dielectric layer. In reality, shear forces usually possess a component that acts normal to the sensor surface, which has the effect of compressing the dielectric layer. This section develops a model that accounts for this effect and describes the angle of the shear force vector in the three dimensional space.

Fig. 4 illustrates the sensor under a shear force F in the three-dimensional space. The force components are resolved into their individual components using the spherical coordinate system.

The initial capacitance of C_1 is given by

$$C_1 = \frac{\epsilon_0 \epsilon_r A_1}{d_1} = \frac{\epsilon_0 \epsilon_r x_1 y_1}{d_1} \quad (15)$$

Given that the shear force changes the overlap area and the distance between the electrodes, we can write the new capacitance for C_1 as

$$C_{1new} = \frac{\epsilon_o \epsilon_r A_2}{d_2} = \frac{\epsilon_o \epsilon_r x_2 y_2}{d_2} = \frac{\epsilon_o \epsilon_r (x_1 + \delta_x)(y_1 + \delta_y)}{d_1 - \delta_d} \quad (16)$$

The change in the differential capacitance for the first differential capacitor is given by

$$\begin{aligned} \Delta C_1 &= C_{1new} - C_1 \\ &= \frac{\epsilon_o \epsilon_r (d_1 y_1 \delta_x + d_1 x_1 \delta_y + d_1 \delta_x \delta_y + x_1 y_1 \delta_d)}{d_1 (d_1 - \delta_d)} \end{aligned} \quad (17)$$

Assuming that the top electrode is well centered over the bottom electrodes, resulting in $x_1 = y_1 = a$, the above equation can be rewritten as

$$\Delta C_1 = \frac{a \epsilon_o \epsilon_r}{d_1} \frac{\left(\delta_x + \delta_y + \frac{\delta_x \delta_y}{a} + a \frac{\delta_d}{d_1}\right)}{1 - \frac{\delta_d}{d_1}} \quad (18)$$

Similarly, the changes in the capacitances for the other differential capacitors are

$$\Delta C_2 = \frac{a \epsilon_o \epsilon_r}{d_1} \frac{\left(-\delta_x + \delta_y - \frac{\delta_x \delta_y}{a} + a \frac{\delta_d}{d_1}\right)}{1 - \frac{\delta_d}{d_1}} \quad (19)$$

$$\Delta C_3 = \frac{a \epsilon_o \epsilon_r}{d_1} \frac{\left(\delta_x - \delta_y - \frac{\delta_x \delta_y}{a} + a \frac{\delta_d}{d_1}\right)}{1 - \frac{\delta_d}{d_1}} \quad (20)$$

$$\Delta C_4 = \frac{a \epsilon_o \epsilon_r}{d_1} \frac{\left(-\delta_x - \delta_y + \frac{\delta_x \delta_y}{a} + a \frac{\delta_d}{d_1}\right)}{1 - \frac{\delta_d}{d_1}} \quad (21)$$

From the above equations,

$$\Delta C_1 + \Delta C_2 + \Delta C_3 + \Delta C_4 = 4 \frac{\epsilon_0 \epsilon_r a^2}{d_1} \frac{\frac{\delta_d}{d_1}}{1 - \frac{\delta_d}{d_1}} \quad (22)$$

$$\Delta C_{average} = C_{initial} \frac{\frac{\delta_d}{d_1}}{1 - \frac{\delta_d}{d_1}} \quad (23)$$

where $\Delta C_{average}$ is the average of the changes in the differential capacitances and $C_{initial}$ is the initial capacitance. Solving for δ_d,

$$\delta_d = d_1 \frac{\Delta C_{average}}{\Delta C_{average} + C_{initial}} \quad (24)$$

The force vector F can be resolved into its components in the three-dimensional space using the spherical coordinate system, which in turn is written in terms of the displacements using Hooke's Law, in the linear regime.

$$F_x = F \sin(\theta) \cos(\phi) = k \delta_x \quad (25)$$
$$F_y = F \sin(\theta) \sin(\phi) = k \delta_y \quad (26)$$
$$F_z = F \cos(\theta) = k \delta_d \quad (27)$$

where θ is the angle of inclination angle, ϕ is the angle of rotation and k is the spring constant of the dielectric layer.

Substituting the *z*-axis relation, the above equation can be rewritten to obtain the angle of inclination of the force.

$$\cos(\theta) = \frac{d_1 k}{F} \frac{\Delta C_{average}}{\Delta C_{average} + C_{initial}} \quad (28)$$

This is rewritten as

$$\theta = \cos^{-1}\left(\frac{d_1 k}{F} \frac{\Delta C_{average}}{\Delta C_{average} + C_{initial}}\right) \quad (29)$$

In the three-dimensional case, the analytical solution for the shear force angle shows a reliance on the values of all four differential capacitances and the spring constant of the dielectric layer, which would require separate analysis, prior to developing angle detection algorithms. It should be noted that the ratio of the spring constant k to the magnitude of the force F can be rewritten as the effective displacement of the sensor electrodes. However, even this would require an accurate experimental setup to determine the displacement of the top electrode with respect to the bottom electrodes of the unit cell.

In the case of a normal force, all four differential capacitances change at the same rate. As a result, $\Delta C_{average} = \Delta C_1$ and $C_{initial} = C_1$. In addition, from Hooke's law, the normal force is proportional to the vertical compression of the dielectric layer i.e. δ_d. The above equation then becomes

$$\begin{aligned} \theta &= \cos^{-1}\left(\frac{d_1}{\delta_d} \frac{\Delta C_1}{\Delta C_1 + C_1}\right) = \cos^{-1}\left(\frac{d_1}{\delta_d} \frac{C_{1new} - C_1}{C_{1new}}\right) \\ &= \cos^{-1}\left(\frac{d_1}{\delta_d} \frac{\delta_d}{d_1}\right) = 0°, \quad \text{as expected.} \end{aligned} \quad (30)$$

The relationship between the components of the applied force and the change in capacitance can be derived as

$$F_x = ka \left[\frac{\Delta C_1 + \Delta C_3}{2C_1} - \frac{\Delta C_{average}}{\Delta C_{average} + C_{initial}}\right] \quad (31)$$

$$F_y = ka \left[\frac{\Delta C_1 + \Delta C_2}{2C_1} - \frac{\Delta C_{average}}{\Delta C_{average} + C_{initial}}\right] \quad (32)$$

$$F_z = kd_1 \left[\frac{\Delta C_{average}}{\Delta C_{average} + C_{initial}}\right] \quad (33)$$

V. DIELECTRIC LAYER MEASUREMENTS

The three-dimensional model for the shear force angle demonstrates that there is a strong dependence of the analytical solution for the detected angle on the relative permittivity of the dielectric layer. In addition, the design and material choice of the dielectric layer play an important role in determining the properties of the sensor such as its sensitivity, detection range and starting operation point. A solid dielectric film has a limited ability to shear, resulting in a restricted shear force measurement. To counter this, the sensor dielectric layer is patterned as posts measuring a few millimeters in thickness. The thickness of the flexible dielectric allows us to stay in the elastic regime, while the patterned structures provide surfaces that can deform and recover easily in response to either a shear or a normal deformation. The patterning of the dielectric structure also allows fort the tune the mechanical properties of the dielectric layer. For a given dielectric material, the various dielectric parameters such as the shape of posts, fill factor, height and diameter affect both the electrical (dielectric constant) and mechanical properties (force response) of the device. This work used Ecoflex-30 as the sensor dielectric material because of its material properties and its easiness to work with.
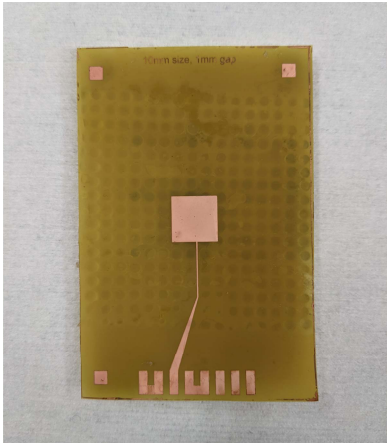
Fig. 5. Fabricated parallel plate capacitor test fixture used for the characterization of the dielectric layer. The capacitor plate has a side length of 10mm.

A. Determination of Relative Permittivity of Bulk Ecoflex-30

Existing literature [39]–[41] on the experimental characterization of Ecoflex-30 places its relative permittivity in a broad range between 2.6 and 3.4. Consequently, to establish a baseline for the dielectric layer measurements, we first determined the relative permittivity of Ecoflex-30 using a simple parallel plate test fixture. Different final weights of Smooth On Inc. Ecoflex-30 silicone mixtures (30gms, 20gms and 10gms) were made by mixing equal parts of Ecoflex-30 Part A and Part B to achieve the final weights. The mixture was stirred vigorously for a few minutes to ensure uniform mixing and poured into a petri dish and degassed in a vacuum chamber to eliminate trapped air bubbles. The silicone was then cured at 75°C for two to three hours, following which the solid Ecoflex layer was removed from the petri dish and trimmed to size to fit a parallel plate capacitor with sides 10mm by 10mm. The top and bottom electrode layers were aligned using a 3D printed jig. Fig. 5 shows an image of a fabricated parallel plate capacitor test structure, where each plate is 10mm by 10mm. An AD7746 (Analog Devices, MA) evaluation board was used to conduct the measurements in the single ended mode, with a 32 Hz excitation signal and a conversion time of 109.6 ms, allowing for an effective resolution of 4aF (up to 21 ENOB).

We observed that the average value of the relative permittivity of Ecoflex-30 was around 2.8. For the 10gm mixture, the measured thickness of the dielectric layer was 1.443mm, leading to a relative permittivity of 2.772. For the 20gm mixture, the measured thickness of the dielectric layer was 2.09mm, resulting in a relative permittivity of 2.862. For the 30gm mixture, the measured thickness was 3.54mm, resulting in a relative permittivity of 2.807. In each measurement, the thickness of the dielectric was measured in multiple locations to account for fabrication variations and a final average value was calculated to ascertain the bulk relative permittivity.

B. Analytical Expression for the Relative Permittivity of the Patterned Dielectric Layer

In this section, we characterize the effects of the geometrical parameters of the patterns on the effective dielectric constant

of the device. The dielectric layer was fabricated by patterning Smooth-On Ecoflex-30 with posts using a 3D printed mold and curing it on a hot plate at 75°C for three to four hours. By using molds with patterns of different physical dimensions, the post dimensions could be varied.

The dielectric pattern can be viewed as an alternating series of a high permittivity material (Ecoflex-0030) with a low permittivity material (air) with a pre-determined fill factor (FF), where the FF is defined as the ratio of the ratio of the area of a post to the total area of the posts and airgaps. A single post and the accompanying space can be considered to be two alternating dielectrics. Consequently, they can be considered as two capacitors in parallel and the following result is obtained

$$C = \frac{\epsilon_0 \epsilon_{r_1} A_1}{d} + \frac{\epsilon_0 \epsilon_{r_2} A_2}{d} \qquad (34)$$

where ϵ_{r_1} corresponds to the relative permittivity of the high permittivity material, ϵ_{r_2} the permittivity of the low index material, A_1 the cross sectional area of the high permittivity material, A_2 the cross sectional area of the low permittivity material and d the thickness of the dielectric material. The entire dielectric layer can be visualized as an alternating series high and low permittivity posts, which implies a series of capacitors with different relative permittivities in parallel. The overall capacitance of the device can be expressed as the total sum of the capacitance of all the posts and airgaps.

$$C_{device} = n_1 \frac{\epsilon_0 \epsilon_{r_1} A_1}{d} + n_2 \frac{\epsilon_0 \epsilon_{r_2} A_2}{d} \qquad (35)$$

where n_1 corresponds to the number of posts and n_2 the number of airgaps.

Using the definition of the fill factor, we can define it as

$$n_{FF} = \frac{n_1 A_1}{n_1 A_1 + n_2 A_2} = \frac{n_1 A_1}{A} \qquad (36)$$

The capacitance for the equation can be re-written in terms of the fill factor as

$$C_{device} = n_{FF} A \frac{\epsilon_0 \epsilon_{r_1}}{d} + (1 - n_{FF}) A \frac{\epsilon_0 \epsilon_{r_2}}{d} \qquad (37)$$

Finally, the analytical expression for the effective permittivity of the dielectric layer of the sensor is written as

$$\epsilon_{device} = n_{FF} \epsilon_{r_1} + (1 - n_{FF}) \epsilon_{r_2} = n_{FF} \epsilon_{r_{post}} + (1 - n_{FF}) \epsilon_{r_{airgap}} \qquad (38)$$

From this expression for the relative permittivity of the sensor dielectric layer, we make the following observations:
- The relative permittivity depends only on the FF (or the overall ratio of the high permittivity material to the low permittivity materials) and not the individual dimensions of the posts.
- While the initial capacitance will vary with the height of the posts, the relative permittivity is the same for posts with identical widths and spacing but different heights.

Keeping these factors in mind allows us to tune the device specifications as per application requirements.

TABLE I
AVERAGE MEASURED VALUES OF THE CAPACITANCE AND THICKNESSES FOR DIFFERENT WEIGHTS OF ECOFLEX-30 AND
CALCULATED AND ANALYTICAL VALUES OF THE RELATIVE PERMITTIVITY

Diameter (mm)	Spacing (mm)	Height (mm)	Fill Factor (%)	Average Measured Height (mm)	Average Measured Capacitance (pF)	Experimentally determined value of Relative Permittivity	Analytical Relative Permittivity (Bulk permittivity = 2.8)	Error between experimental and analytical results (%)
2	1	2	66.67	3.3302	0.5761508	2.14869	2.2	2.387967
1	1	2	50	3.478	0.4724268	1.855772	1.9	2.383267
2	2	2	50	3.604	0.4794496	1.951588	1.9	-2.64339
1	1	4	50	4.51	0.365523	1.86188	1.9	2.047393
2	1	4	66.67	5.104444	0.3771204	2.174147	2.2	1.18911

C. Experimental Determination of the Relative Permittivity of the Patterned Dielectric Layer

To experimentally determine the relative permittivity of the sensor dielectric layer, we utilized a parallel plate capacitor test fixture, similar to the one used to experimentally determine the bulk dielectric constant of Ecoflex-30. Samples of the dielectric layer with different FFs and post heights were fabricated by molding Smooth On Inc. Ecoflex-30 using 3D printed molds. The parallel plate capacitors were fabricated using the same fabrication process mentioned earlier. The square capacitor plates had a side of 10mm and consequently an overlap area of 100mm^2. The top and bottom electrode layers were once again aligned using a 3D printed jig. The capacitance was then measured using the same Analog Devices AD7746 Evaluation board as used in the previous section with the same settings. Each measurement comprised of capturing 1000 capacitance data points and the measurement was repeated multiple times to obtain an average capacitance value. The thickness of the dielectric layer was ascertained in multiple locations to account for fabrication variations and measurement errors arising due to compression of the dielectric while measuring the thickness, and an average thickness was calculated.

Table I shows the results of the experimentally determined data, along with the analytical and simulation results. We observe that the experimental results are in good agreement with the analytical results, with the largest deviation being in the range of 2.6% for Row 3 of the table for the analytical results. The variations in the measured value largely come from the inability to measure the thickness of the dielectric layer, without compressing it.

VI. RESULTS

To understand the impact of normal and shear forces on the sensor in detail, we looked at the characterization of the sensor in two ways. First, we looked at the local force response of a single unit cell and its performance under both a normal force and shear forces at different angles. We then repeated the experiments to characterize the normal and shear force

responses at a global level, i.e., at the level of a subset of the sensor array.

In order to characterize the shear sensor array, we custom built a microcontroller based serial data acquisition system that allows for the sequential scanning and measurement of the multiplexed differential capacitors and the logging, data processing and visualization in real time. The custom data acquisition system was built around the AD7745 (Analog Devices, MA), a Capacitance to Digital convertor based on sigma delta modulation and having a single capacitance input channel. The chip has a resolution of up to 10^{-18}F (ENOB of 21 bits), an accuracy of 10^{-15} F and can measure a full scale (changing) capacitance range of ±4pF.

The capacitive unit cell structure has a single top electrode for a set of four bottom electrodes, resulting in an asymmetric structure that necessitates the careful design of a multiplexed readout circuit. We developed a multiplexed readout scheme comprising of mux/demux chips and grounding switches that connects each differential capacitor top and bottom electrode pair in the unit cell to the AD7445 excitation and capacitance input through a low resistance path when it has to be polled, while grounding all the other differential capacitor plates, as shown in Fig. 6. The data acquisition system was designed to have 16 read channels each for the top and bottom electrodes, allowing us to read up to 256 differential capacitors sequentially. The board can be easily be scaled up to accommodate a larger number of electrodes. A four layer PCB was used in order to improve the EMI performance.

The PCB polling and read methods are controlled by an Arduino based microcontroller (Arduino Mega 2560) that communicates with the board using the I^{2}C protocol. In order to address the top and bottom electrodes efficiently (both in terms of switching noise and digital read/write speed), the Port Registers on the Arduino were used to address the Texas Instruments CD74HC4515 Multiplexer/Demultiplexer chips. The chip is set to act as a demultiplexer for the AD7745 excitation signal to the bottom electrodes and as a multiplexer to the top electrode lines of the sensor for the AD7745 Capacitive input channel. CD74HC4515 decoders that are also addressed by the Arduino Port Registers are used
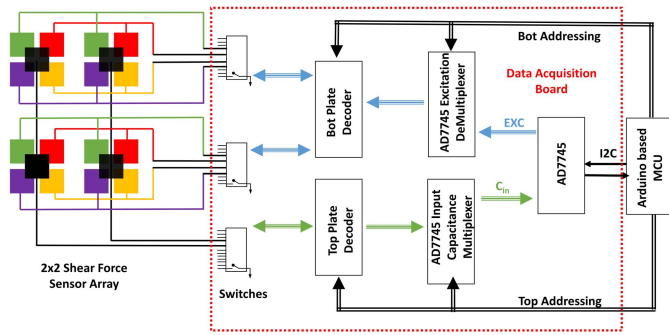
Fig. 6. Schematic illustrating the sensor array and the logical layout of the data acquisition board with the individual components.

to connect the mux/demux lines to the sensor via a series of Analog Devices ADG712 switches. These switches have a low resistance, quick switching time and connect the lines to ground when a logic high signal is applied, which further aids with improving performance by reducing the amount of cross coupling (cross talk and fringing capacitance) between the capacitors in each unit cell. We used Matlab to serially acquire the data from the Arduino and process and plot it in real time.

A. Performance of a Single Unit Cell

We first examined the performance of a single Unit Cell in the multiplexed force sensor array and ascertained the effects of a local force on that unit cell and other unit cells in the vicinity.

For ease of fabrication, we chose electrode dimensions of 3mm × 3mm, with an electrode gap of 2mm (resulting in a capacitor overlap of 1mm each side). The parameters for the Ecoflex-30 dielectric were chosen to be 2mm in diameter, 2mm in spacing (50% duty cycle) and 2mm in post height.

The sensor array was affixed to a tilt stage, whose angle could be changed in increments of 15°. A Shimpo FG7000 series force gauge mounted on a movable z-axis stage was used to measure the force applied to the sensor array. A small block of PDMS that was completely cured at 100°C for 5 to 6 hours was used to distribute the force onto the unit cell. The tilt angle of the sensor results in a shear force being applied to the sensor from the right to the left. We designed calibration routines to account for board and cable parasitics using the capacitive offset and CAPDAC registers on the AD7745 chip. This routine also zeroed out the initial capacitances on all the differential capacitors.

As an example for these measurements, we picked Unit Cell 5. We are interested in the linear region of the force vs capacitance response. Fig. 7 shows the results of the measurements when the sensor is at tilted at angles of (a) 0°, (b) 15°, (c) 30° and (d) 45°. The top row shows the plots of the capacitance vs force data with a linear fit, where the slopes indicate the relative sensitivities of each of the differential capacitors in Unit Cell 5. The middle row shows the capacitance vs force data fitted to a quadratic curve, for a better approximation of the data and representation of the saturation in the capacitance values due to the compression

TABLE II

SLOPES EXTRACTED FROM THE CAPACITANCE vs FORCE DATA FOR THE FOUR DIFFERENTIAL CAPACITORS IN UNIT CELL 5, USING A FIRST ORDER APPROXIMATION, FOR A NORMAL FORCE AND FOR TILT ANGLES OF 15, 30 AND 45 DEGREES

Tilt Angle	Bot Left (fF/N)	Top Left (fF/N)	Bot Right (fF/N)	Top Right (fF/N)	Left (fF/N)	Right (fF/N)
0°	4.9831	4.3769	4.9456	4.3308	4.68 ± 0.428648	4.6382 ± 0.434729
15°	4.7786	5.226	3.8069	3.3902	5.0023 ± 0.31636	3.59855 ± 0.294651
30°	5.3868	5.3489	3.5331	3.4735	5.36785 ± 0.267993	3.5033 ± 0.421436
45°	6.2233	6.2455	3.9979	3.7674	6.2344 ± 0.156978	3.88265 ± 0.162988

TABLE III

AVERAGE CAPACITANCE VALUES OF UNIT CELL 5 AT 15N (SATURATION REGION) IN RESPONSE TO DIFFERENT TILT ANGLES, AS WELL AS THE MAXIMUM AVERAGE IN THE SURROUNDING UNIT CELLS, GIVING US AN IDEA OF THE MARGINS FOR THRESHOLDING SIGNALS

Tilt Angle	Left Average Capacitance (fF)	Right Average Capacitance (fF)	Surrounding Unit Cells Max Average (fF)	Noise Margin (fF)
0°	70.98	70.98	14.8	56.18 L, 56.18 R
15°	73.74	50.25	8	65.74 L, 42.25 R
30°	78.34	48.76	11.5	66.84L, 37.26R
45°	81.17	48.975	22.6	58.57 L, 26.375 R

of the dielectric layer. The bottom row shows a snapshot of the spatial distribution of the capacitance values of the sensor array at a force of 10N.

Table II shows an overview (characteristics were quantified in terms of the slopes of the first order fitted data) of the capacitance vs force data for Unit Cell 5 for the different tilt angles. In the case of a normal force, i.e., 0° tilt, all four differential capacitors show a uniform change in their differential capacitances with the applied force. The slight variations in the slopes of the normal force response can be attributed to fabrication defects in the dielectric layer (both thickness variations and variations in the post parameters affecting local effective permittivity values) and alignment variations between the top and four bottom electrodes, resulting in minor changes in the overlap area. When the sensor was tilted at an angle of 15°, the left electrode pair show a marked increase in the capacitance data signal slope as compared to the right pair, which is indicated by a separation in slopes of 1.40375 fF/N.
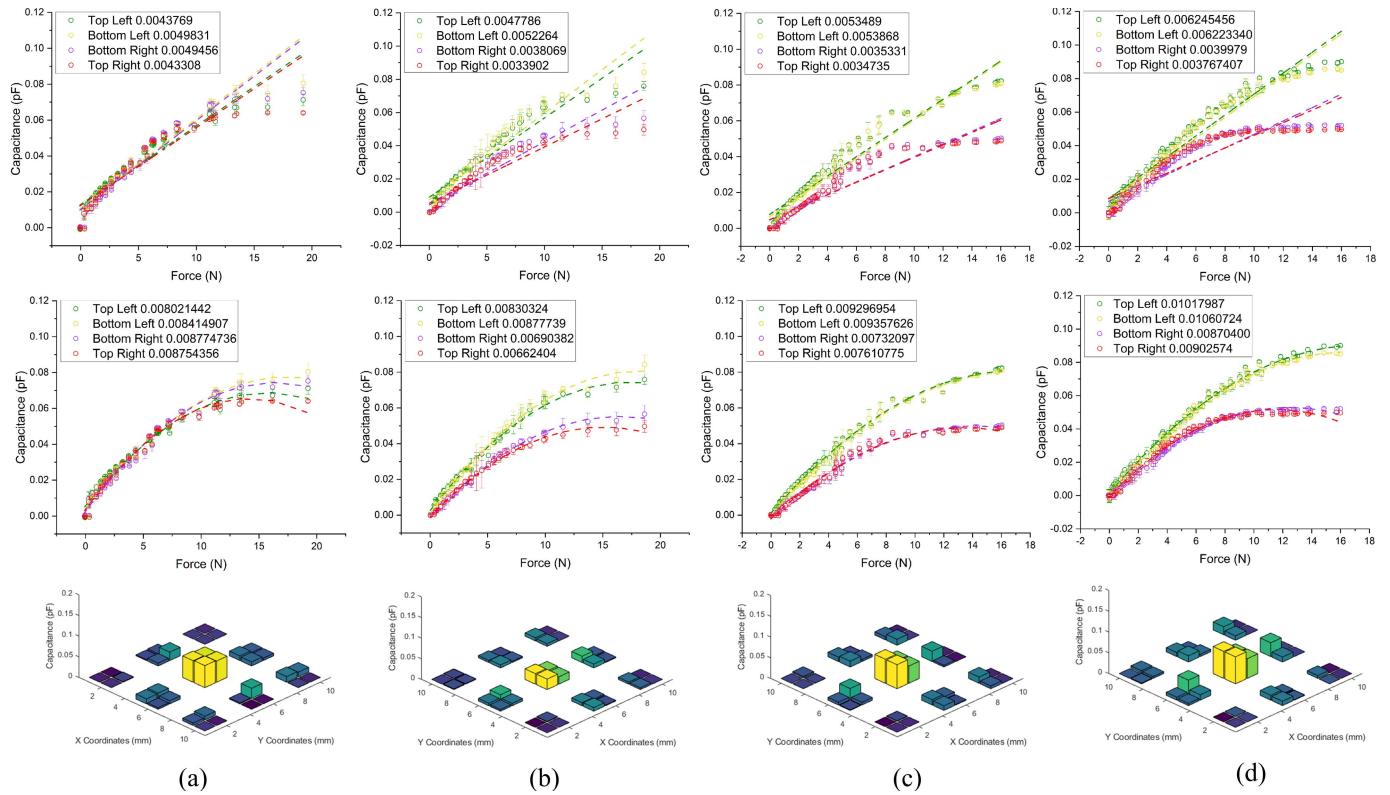
Fig. 7. Capacitance vs Force plots for Unit Cell 5 in the force sensor array for a local force applied at Unit Cell 5. The top row indicates the fit for all four differential capacitances using a linear model, the middle row indicates the fit for all the four differential capacitances using a quadratic model and the bottom row shows a snapshot of the spatial distribution of the differential capacitances for the entire array at a force of 10N. (a) Normal Force (b) Shear Force from the right to the left at an angle of 15°. (c) Shear Force from the right to the left at an angle of 30°. (d) Shear Force from the right to the left at an angle of 15°. The tilt results in a shear force being applied from right to left.

This separation increases to 1.8637 fF/N and 2.35175 fF/N for tilts of 30° and 45°. The individual top and bottom differential capacitors on the left and right respectively show good uniformity within an acceptable error range.

The quadratic fit of the capacitance *vs* force data reveals the non-linear behavior of the Ecoflex-30 dielectric layer. We observed that there is a region of linearity until around 10N, beyond which the capacitance value begins to saturate, both for the normal forces and the shear force cases. This can be attributed to the complete compression of the dielectric layer. Consequently, in order to measure larger force ranges, a dielectric layer that has a higher Young's Modulus should be used.

B. Unit Cell Cross Talk/Noise Margin

The bottom row in Fig. 7 shows the spatial distribution at a 10N snapshot of all the differential capacitances in the sensor array when both a normal force and a shear force was applied locally to Unit Cell 5. In order to ascertain the amount of cross talk amongst the unit cells, when a local force is applied to Unit Cell 5, we describe the margins observed between the capacitors in Unit Cell 5 and the other Unit Cells in the vicinity under different loading scenarios.

The following are observed

- For the 0° tilt case (normal force), the average value of all the four differential capacitors in the Unit Cell

being 56.5 fF. In comparison, the maximum average value amongst the surrounding unit cells is 9.1 fF, resulting in a margin of 42.31 fF.

- For a tilt of 15°, Unit Cell 5 has an average left capacitance value of 64.15 fF and an average right capacitance value 44.58 fF. In contrast, the maximum average capacitance value amongst all the other Unit Cells is 7.6 fF, resulting in margins of 56.55 fF and 36.78 fF for the left and right differential capacitances in Unit Cell 5.

- For a tilt angle of 30°, these margins are 54.61 fF and 35.18 fF for the left and right differential capacitances in Unit Cell 5

- For a tilt angle of 45°, these margins are 53.46 fF and 31.29 fF for the left and right differential capacitances in Unit Cell 5.

Table III shows the values of the left and right differential capacitances for Unit Cell 5 at different tilt angles in the region of saturation, i.e., at a 15N force snapshot (saturation region of the capacitances). The table also describes the maximum values of the differential capacitances in the surrounding unit cells and the subsequent nose margins for the left and right differential capacitance pairs. In this case also, we observed good noise margins, indicating that the local application of an increasing force to a Unit Cell does not adversely affect the performance of the sensor array. The threshold margins are quite large for both normal and shear forces, allowing us to

(a)   (b)   (c)
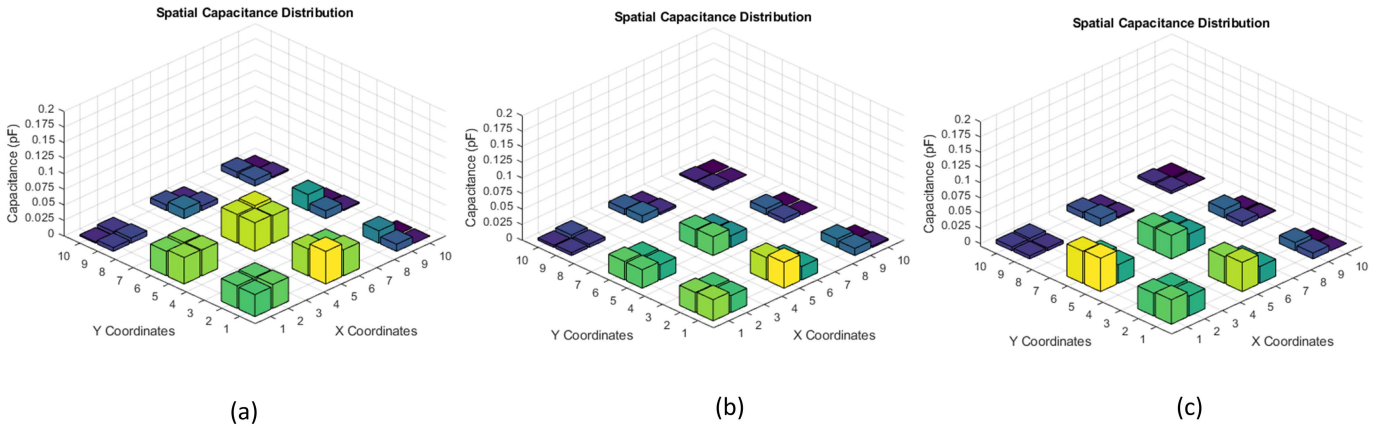
Fig. 8.   Capacitance vs Force plots for the sensor array when a force is applied across Unit Cells 4, 5, 7 and 8. The figures capture the snapshots of a 15N force applied when the sensor has a tilt of (a) 0°, (b) 15°, and (c) 30°. The tilt results in a shear force being applied to the sensor from right to left.

TABLE IV

AVERAGE CAPACITANCE VALUES OF UNIT CELLS 4, 5, 7 AND 8 AT 15N (SATURATION REGION) IN RESPONSE TO DIFFERENT TILT ANGLES,
AS WELL AS THE AVERAGE OF THE MAXIMUM CAPACITANCE IN THE SURROUNDING UNIT CELLS

Tilt	Unit Cell C4 Left Average Capacitance (fF)	Unit Cell C4 Right Average Capacitance (fF)	Unit Cell C5 Left Average Capacitance (fF)	Unit Cell C5 Right Average Capacitance (fF)	Unit Cell C7 Left Average Capacitance (fF)	Unit Cell C7 Right Average Capacitance (fF)	Unit Cell C8 Left Average Capacitance (fF)	Unit Cell C8 Right Average Capacitance (fF)	Surrounding Unit Cells Max Average (fF/N)
0°	41	41	45	45	39	39	45.5	44	10
15°	29.7	21.7	29.4	18.1	33.1	24.7	35.8	21.2	4.9
30°	49.8	32.2	40.4	27.3	39.8	27	45.8	26.3	6.1

TABLE V

NOISE MARGINS FOR UNIT CELLS 4, 5, 7 AND 8 AT 15N (SATURATION REGION). THE NOISE MARGINS WERE CALCULATED BY TAKING THE LOWER
CAPACITANCE VALUE (WHICH IN THIS EXPERIMENT IS THE AVERAGE OF THE TOP LEFT AND BOTTOM LEFT CAPACITANCES)
AND SUBTRACTING IT FROM VALUE IN THE RIGHTMOST COLUMN IN TABLE IV

Tilt	Noise Margins for Unit Cell 4 (fF)	Noise Margins for Unit Cell 5 (fF)	Noise Margins for Unit Cell 7 (fF)	Noise Margins for Unit Cell 8 (fF)
0°	31 L, 31 R	35 L, 35 R	29 L, 29 R	35.5 L, 34 R
15°	24.8 L, 16.8 R	24.5 L, 13.2 R	28.2 L, 19.8 R	30.9 L, 16.9 R
30°	43.7 L, 26.1 R	34.3 R, 21.2 L	33.7 L, 20.9 R	39.7 L, 20.2 R

effectively localize the force, based on the capacitance signal data.

C. Array Performance

We looked at the performance of the sensor when a global shear force was applied across multiple unit cells. A similar procedure was followed as when testing the single unit cell, with the exception of using a larger block of PDMS to apply the force over multiple unit cells.

Fig. 8 shows the 15N snapshot of the spatial distribution of the unit cell differential capacitances when a force was applied to Unit Cells 4, 5, 7 and 8. Fig 9 (a) shows the case when a normal forces was applied. Fig 9 (b) shows the case when the force was applied while the sensor was tilted at an angle of 15 degrees and (c) when the sensor was tilted at an angle of 30 degrees.

Table IV shows the average right and left capacitances for Unit Cells 4, 5, 7 and 8, and corresponding average value of the maximum capacitance in the surrounding Unit Cells (Unit Cells 1, 2, 3, 6 and 9) under normal and shear loading. The average value of the capacitance in the surrounding Unit Cells allows for the determination of the noise margins in the Unit Cells under test.

Table V shows the noise margins for Unit Cells 4, 5, 7 and 8. For the given data, the noise margins were calculated by taking the lower capacitance value (which in this experiment is the average of the top left and bottom left capacitances) and subtracting it from the maximum average capacitance of the surrounding Unit Cells

- For a tilt of 0°, we observe that the left and right different capacitances in each unit cell have similar responses. The noise margins between the Unit Cells under force and the
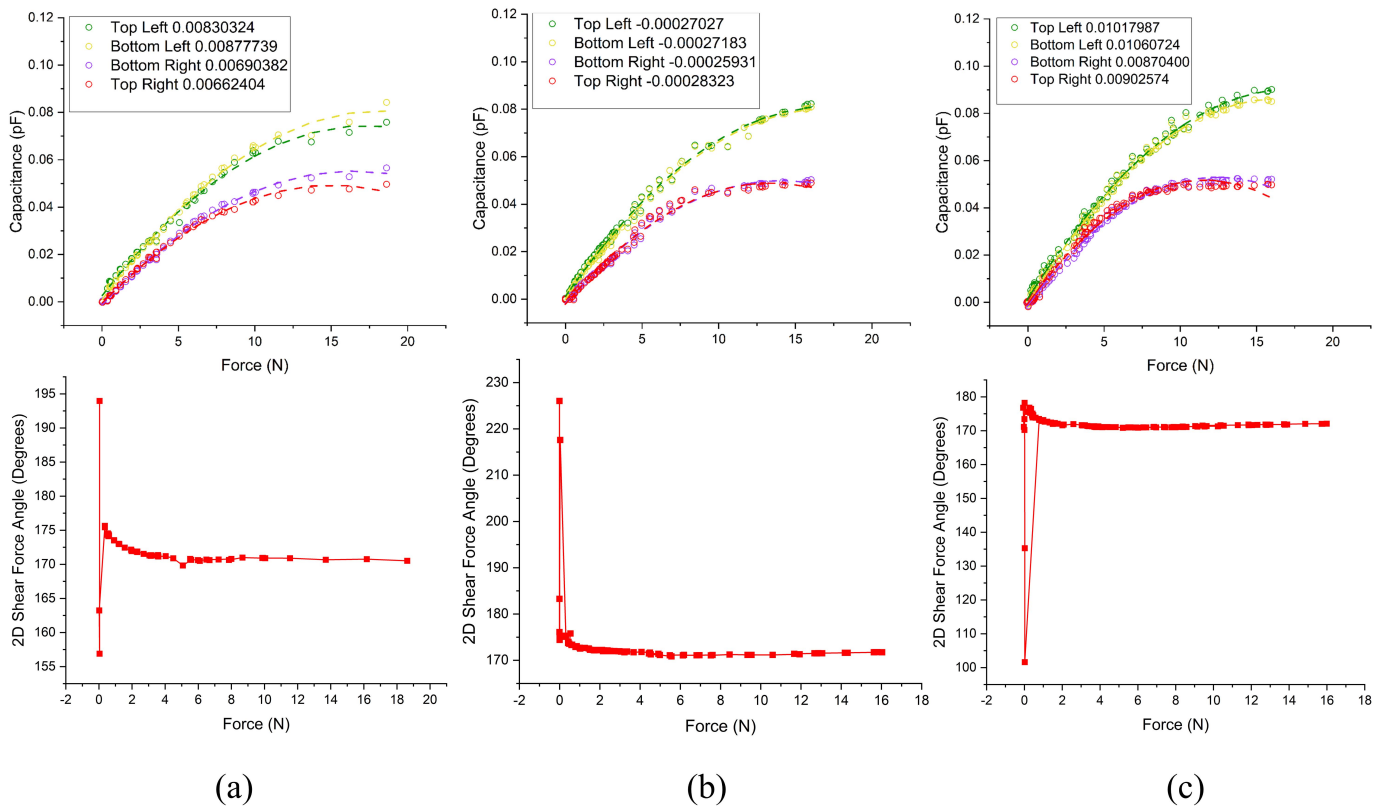
Fig. 9. Estimation of the shear force angle in two dimensions from the experimental data for Unit Cell 5 for a tilt angle of (a) 15 degrees (b) 30 degrees and (c) 45 degrees. The tilt results in a shear force being applied to the sensor from right to left.

surrounding Unit Cells is about 29fF at the minimum and 35.5fF at the maximum.

- For a tilt of 15°, the left differential capacitances show a separation about 11fF on average from the right differential capacitances. The noise margins between the Unit Cells under force and the surrounding Unit Cell are about 16.5fF on average (considering the lower values from the left differential capacitances).

- For a tilt of 30°, the left differential capacitances show a separation of about 16fF on average from the right differential capacitances. The noise margins between the Unit Cells under force and the surrounding Unit Cell are about 22 fF on average (considering the lower values from the left differential capacitances).

We thus see that the sensor is capable of discerning between global forces applied across a number of unit cells. In particular, it is possible to discern between normal and shear forces with relative ease and between shear forces that are applied at different angles. This would allow for the development of detailed predictive models for applied forces, based on the changes in the differential capacitances across the entire array.

D. Unit Cell Angle Estimation

Fig. 9 shows the two-dimensional shear force angle that was extrapolated from the experimental data for Unit Cell 5 at the different tilt angles of (a) 15 degrees (b) 30 degrees and (c) 45 degrees. The tilt results in a shear force from right to left, increasing the values of the left differential capacitances

of the unit cell. The angle is ascertained as 0° for the first quadrant (shear from left to right) and 180 for the second quadrant (shear from right to left). The above experimental results show good agreement with the two-dimensional model with an error of around 5° on average. The spikes in the two-dimensional angle data at the beginning can be attributed to the initial compression of the dielectric layer when the probe is lowered, which is not accounted for in the two dimensional model.

Fig. 10 shows the simulated results when an in plane force is applied at the top electrodes of the sensor at an angle of (a) 0°, (b) 30° and (c) 45°. It is observed that the relative direction of the force can be easily determined by looking at the behavior of the individual differential capacitances. For example, in the case of an angle of 0°, an increase in both C_1 and C_3 is expected along with a decrease in C_2 and C_4. In contrast, for the 45° case, we would expect an increase in C_1, a decrease in C_4 and no significant changes in C_2 and C_3. Using the model developed in Section IV, we were able to estimate the in plane angle from the differential capacitance data, within an error of 1°.

Fig. 11 shows the simulated results when an out of plane shear force was applied to the sensor. The extraction of the three dimensional angle requires the experimental determination of the spring constant of the patterned dielectric layer, which is beyond the scope of this work. We consequently estimated the spring constant from the simulation results by calculating the effective displacement of the dielectric material in each of the Cartesian directions. A force was applied that
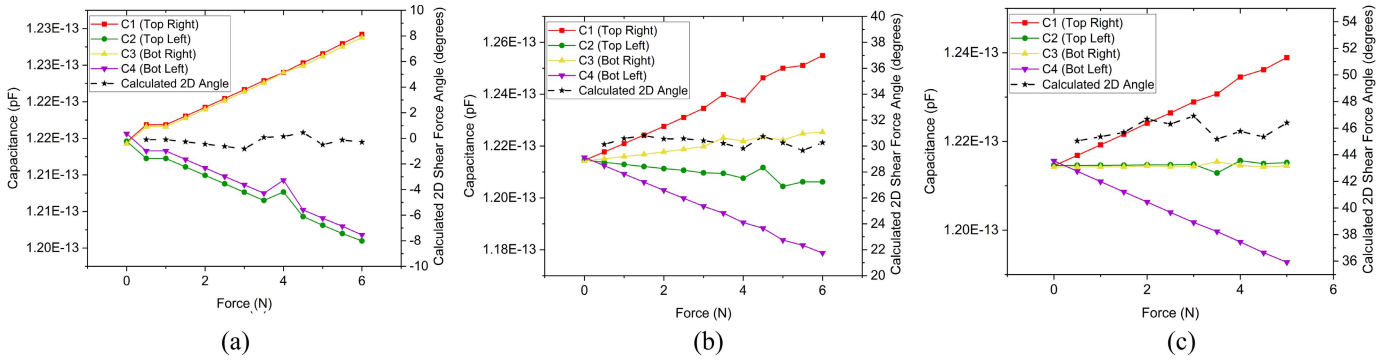
Fig. 10.   Simulation results for the estimation of the two dimensional (in plane) for Unit Cell 5 for an in-plane shear angle of (a) 0 degrees (b) 30 degrees and (c) 45 degrees.
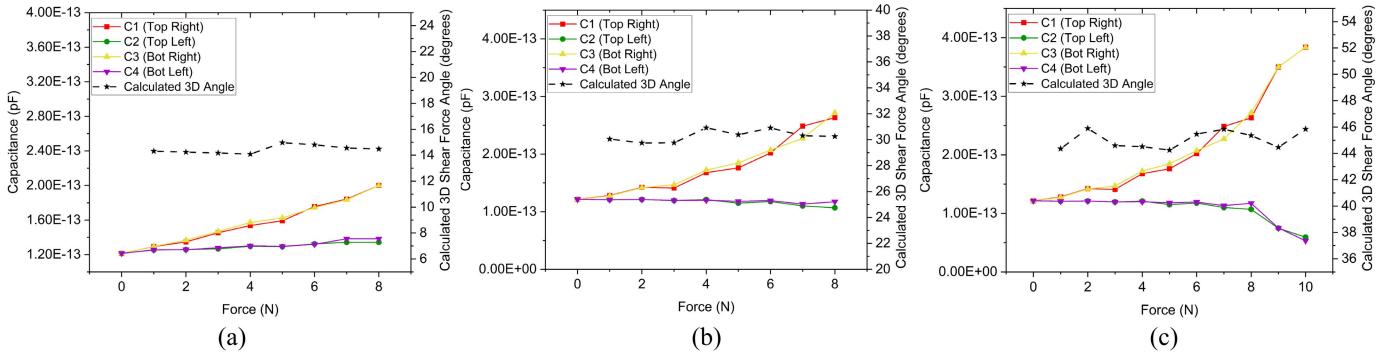

Fig. 11.   Simulation results for the estimation of the three-dimensional shear force angle (inclination) for Unit Cell 5 for a tilt angle of (a) 15 degrees (b) 30 degrees and (c) 45 degrees. In all three cases, the in-plane angle was taken to be 0 degrees.

had an in plane component of $0°$ in the direction of C_1 and C_3 and we varied the out of plane angle from $0°$ to $45°$, in steps of $15°$. Fig 11 (a) shows the result for an angle of $15°$, (b) $30°$ and (c) $45°$. The error in the estimated angle for each of the cases is within $2°$ for each of these cases.

E. Cyclic Loading

Cyclic testing was conducted on Unit Cell 5 of the array to assess the repeatability of the sensor output, under the same shear force conditions that were used in the previous experimental sections. The sensor was setup on a tilt stage at 0 degrees and then loaded with incremental force steps until 5N, following which the force was released in decreasing steps, until complete unloading is achieved. This was repeated for tilt angles of 15 degrees, 30 degrees and 45 degrees.

Fig. 12 shows the results of five cycles of cyclic loading and unloading for (a) 0 degrees (b) 15 degrees (c) 30 degrees and (d) 45 degrees of tilt. In each of the cases, the data indicates a highly reproducible sensor output, with minimal variations over cycles. The difference between the right and left set of electrodes is marked in each case, with the difference increasing from (a) to (d), indicating the increasing shearing force from right to left as the tilt angle is increased.

F. Constant Forces

The behavior of the sensor under a constant applied force was conducted to assess the stability of the sensor output, as well as to ascertain the SNR of the sensors. We repeated the

experiment under similar conditions to Section E viz. loading from 0 to 5N in incremental steps at different tilt angles, with the only difference being that each step was held for 60 seconds.

Fig. 13 shows the capacitance data for tilts of (a) 0 degrees, (b) 15 degrees, (c) 30 degrees and (d) 45 degrees for slowly incrementally loaded forces up to 5N. In each case, the sensor output is quite stable with the average standard deviation at each step being two orders of magnitude lower than the measured data. We also calculated the signal to noise ratio (SNR) at each step using the data from current and previous load steps. The calculated average SNR's for loading with 0 degrees tilt is 15, for the 15 degrees tilt is 11, for the 30 degrees tilt is 13 and for the 45 degree tilt is 10.

We also looked at the sensor hysteresis after loading and unloading with a constant set of forces over the 5N range. Fig 13 shows the capacitance data after loading till 5N and then unloading for tilts of (e) 0 degrees, (f) 15 degrees, (g) 30 degrees and (h) 45 degrees. As is expected, there is a small amount of hysteresis, that increases as the tilt angle is increased. This can be attributed to the slow relaxation of the dielectric layer posts under is as the shear load is removed. The observed hysteresis would be lower under smaller shear force loading.

VII. DISCUSSION AND FUTURE WORK

The differential capacitances in each unit cell are subject to variations in their values as a result of fabrication. These can take the form of thickness variations in the dielectric layer,
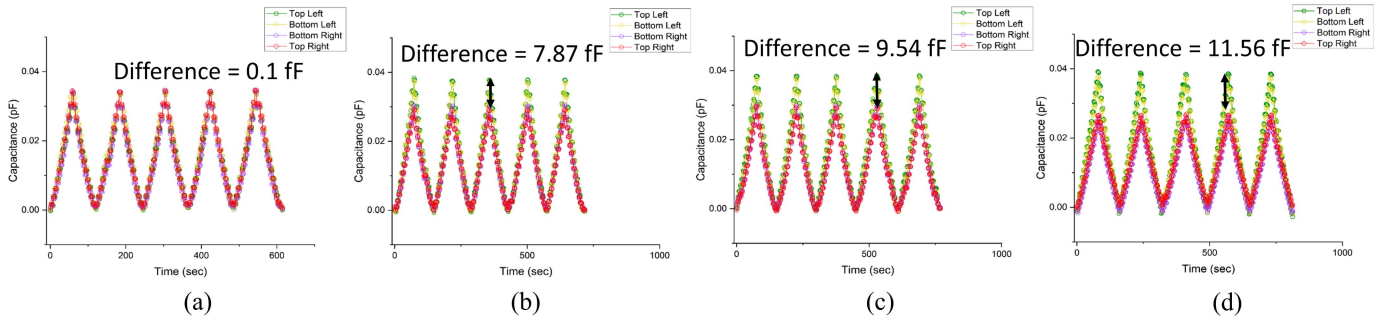
Fig. 12. Cyclic loading of the sensor unit cell from 0N to 5N under tilts of (a) 0 degrees (b) 15 degrees (c) 30 degrees and (d) 45 degrees, with the data for 5 cycles shown. The difference in the right and left capacitances has been demonstrated.
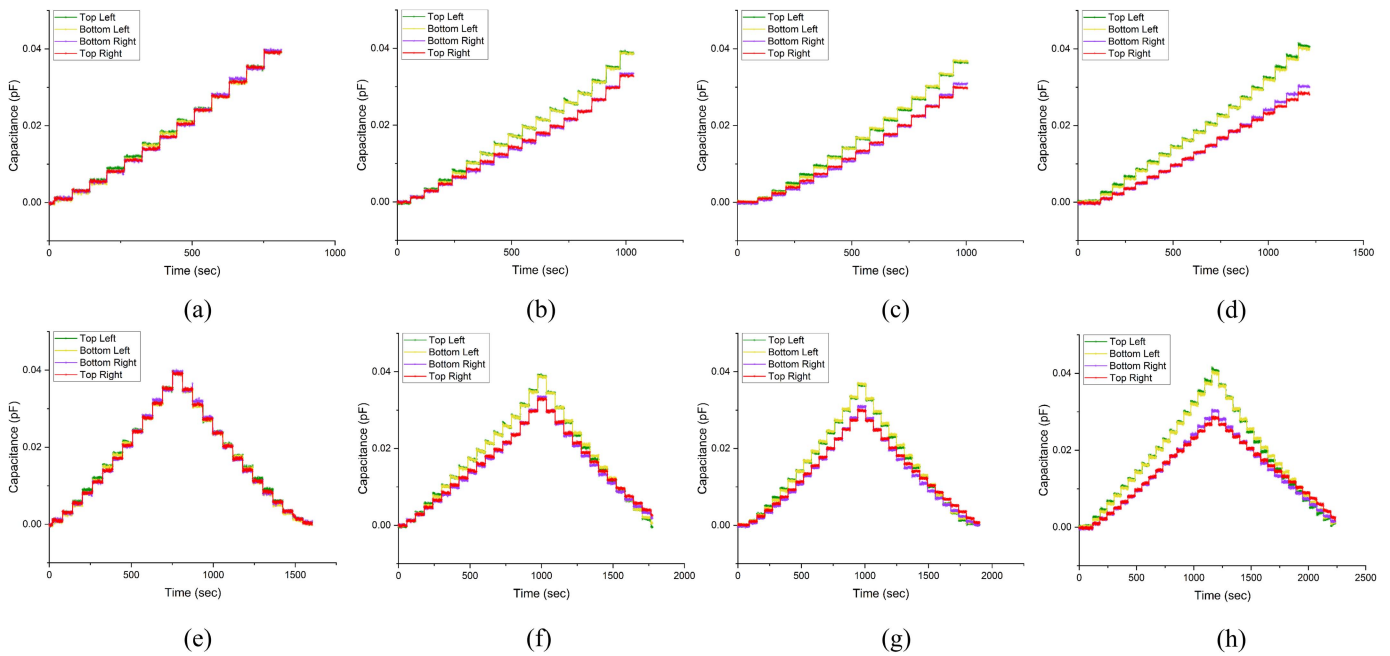

Fig. 13. The top row shows the capacitance plots for incremental loading of the sensor from 0N to 5N for tilt angles of (a) 0 degrees, (b) 15 degrees, (c) 30 degrees and (d) 45 degrees. The bottom row shows the capacitance hysteresis when loading from 0N to 5N and slowly unloaded for tilt angles of (e) 0 degrees, (f) 15 degrees, (g) 30 degrees and (h) 45 degrees.

variations during the curing and peel-off process or in the physical dimensions of the posts as a result of the air bubbles being trapped in the polymer, while pouring. The thickness variations affect the response of the capacitors directly (offsets in the initial capacitance) while the change in post parameters creates non-uniformities in the local dielectric index of the unit cells, affecting the capacitive response. Another source of error is the alignment of the top electrode with respect to the bottom electrode for all the unit cells in the array, which results in overlap area variations. The use of custom alignment marks and holding jigs with posts to physically center the top and bottom electrode layers might help with this. Uniformity in the dielectric layer can be improved by using high resolution molds and hydrophobic coatings, to facilitate the easy release of the dielectric layer from the mold, as well as facilitate the easy movement of trapped air bubbles to the surface.

The estimation of the out-of-plane force angle requires the determination of the spring constant of the patterned dielectric layer. This would entail the detailed mechanical

characterization of the dielectric layer as well as methods to track the displacement of the top electrode layer with respect to the bottom electrode layer in all three axes. In addition, further experiments would have to be conducted to characterize the difference in the compression of the dielectric layer as a result of the normal and shear components of the applied force. The analytical force capacitance model would have to be refined as well.

Another aspect of sensor improvement is designing better shielding strategies to protect the sensor from electromagnetic interference. These would include active shielding at the sensor level, cable and board shielding, and the use of shielded connectors.

Given the applications of this sensor in the measurement of biomechanical metrics, which involve contoured body surfaces, short term future work would involve assessing the sensor performance and its ability to estimate shear force angles along curved surfaces. This would also necessitate the development of ergonomic sensor form factors that can easily

TABLE VI

COMPARISON OF CHARACTERISTICS FROM DIFFERENT STUDIES

	Type	Normal Force				Shear Force				Size	Sensor Spacing	Bump Layer	2D Angle	3D Angle
		Range (mN)	Resolution (mN)	DR	Sensitivity (%/mN)	Range (mN)	Resolution	DR	Sensitivity (%/mN)					
[42]	Resisitive	1470	100	15:1	-	4000	250	16:1	-	1mm	2mm	Yes	No	No
[43]	Capacitive	20	3	6.5:1	1.2	20	3	6.5:1	1.3	2mm	2mm	Yes	No	No
[27]	Capacitive	108	26	4:1	1.67	108	26	4:1	1.67	8mm	8mm	Yes	No	No
[44]	Resistive	500	25	20:1	0.005	5000	150	33:1	0.0012	1mm	4.5mm	Yes	No	No
[45]	Resistive	500	100	5:1	0.006	2000	310	6.5:1	0.086	7mm	8mm	Yes	No	No
[46]	Resistive	500	50	10:1	0.002	5000	250	20:1	0.03	3mm	4.5mm	Yes	No	No
[36]	Capacitive	2000	50	40:1	-	8000	190	42:1	-	1mm	3mm	No	No	No
[47]	Capacitive	100	10	10:1	0.237	150	10	15:1	0.096	5mm	1mm	Yes	No	No
Current	Capacitive	15000	250	60:1	0.04	15000	250	60:1	0.03667	8mm	2mm	No	Yes	Yes

be fitted to fingertips and shoe-insoles. Long-term future work involves the development of more detailed predictive models to determine the individual force components, as well as the shear angle in real-time from the capacitance data. In addition, more work has to be done on the material properties of both the dielectric and the electrode layers to allow the sensor to withstand the large magnitudes of body reaction forces that are seen in everyday scenarios such as slips and falls.

Table VI provides a comparison of the different performance metrics such as range, resolution, dynamic range, sensitivity, overall unit cell size, sensor thickness, presence of a bump layer to facilitate shear and the ability to discriminate between 2D and 3D angles based on the capacitance data of prior published works in this area. While our work has lower sensitivity, we offer a higher dynamic range, no bump layer and the ability to discriminate the 2D and 3D angle based on the capacitance data.

VIII. CONCLUSION

This work presents the development of a highly flexible, robust and compliant sensor array that can measure normal and shear forces with a high level of discernment at both a local and global level. The sensor was fabricated using a simple rapid prototyping process, which allows us to easily tune the sensor and dielectric geometry based on the application requirement. Experiments were carried out to ascertain the bulk permittivity of the dielectric material and these experiments were extended to ascertain the effective relative permittivity of the patterned dielectric layer. In addition, an analytical model for the effective relative permittivity was developed, which showed good agreement with the experimental data and both results were validated by simulations using the data from the experimental results. Models were developed to ascertain the shear force angle in both the two- and three-dimensional cases and the results were validated through the use of FEA simulations.

ACKNOWLEDGMENT

REFERENCES

[1] R. S. Dahiya, G. Metta, M. Valle, and G. Sandini, "Tactile sensing-from humans to humanoids," *IEEE Trans. Robot.*, vol. 26, no. 1, pp. 1–20, Jan. 2009.

[2] A. L. Trejos, J. Jayender, M. Perri, M. Naish, R. Patel, and R. Malthaner, "Robot-assisted tactile sensing for minimally invasive tumor localization," *Int. J. Robot. Res.*, vol. 28, no. 9, pp. 1118–1133, 2009.

[3] P. Maiolino, M. Maggiali, G. Cannata, G. Metta, and L. Natale, "A flexible and robust large scale capacitive tactile system for robots," *IEEE Sensors J.*, vol. 13, no. 10, pp. 3910–3917, Oct. 2013.

[4] J. Platkiewicz, H. Lipson, and V. Hayward, "Haptic edge detection through shear," *Sci. Rep.*, vol. 6, no. 1, p. 23551, Sep. 2016.

[5] J. W. Tappin and K. P. Robertson, "Study of the relative timing of shear forces on the sole of the forefoot during walking," *J. Biomed. Eng.*, vol. 13, no. 1, pp. 39–42, Jan. 1991.

[6] M. Yavuz, G. Botek, and B. L. Davis, "Plantar shear stress distributions: Comparing actual and predicted frictional forces at the foot–ground interface," *J. Biomech.*, vol. 40, no. 13, pp. 3045–3049, Jan. 2007.

[7] J. E. Perry, J. O. Hall, and B. L. Davis, "Simultaneous measurement of plantar pressure and shear forces in diabetic individuals," *Gait Posture*, vol. 15, no. 1, pp. 101–107, 2002.

[8] M. Mimura, T. Ohura, M. Takahashi, R. Kajiwara, and N. Ohura, Jr., "Mechanism leading to the development of pressure ulcers based on shear force and pressures during a bed operation: Influence of body types, body positions, and knee positions," *Wound Repair Regener.*, vol. 17, no. 6, pp. 789–796, Nov. 2009.

[9] L. Rocchi, L. Chiari, M. Mancini, P. Carlson-Kuhta, A. Gross, and F. B. Horak, "Step initiation in Parkinson's disease: Influence of initial stance conditions," *Neurosci. Lett.*, vol. 406, nos. 1–2, pp. 128–132, Oct. 2006.

[10] C. Tard *et al.*, "Attention modulates step initiation postural adjustments in Parkinson freezers," *Parkinsonism Rel. Disorders*, vol. 20, no. 3, pp. 284–289, Mar. 2014.

[11] J. E. Sanders and C. H. Daly, "Normal and shear stresses on a residual limb in a prosthetic socket during ambulation: Comparison of finite element results with experimental measurements," *J. Rehabil. Res. Develop.*, vol. 30, pp. 191–204, Jan. 1993.

[12] M. C. Hsieh *et al.*, "A contact-type piezoresistive micro-shear stress sensor for above-knee prosthesis application," *J. Microelectromech. Syst.*, vol. 10, no. 1, pp. 121–127, Mar. 2001.

[13] A. F. T. Mak, M. Zhang, and D. A. Boone, "State-of-the-art research in lower-limb prosthetic biomechanics-socket interface: A review," *J. Rehabil. Res. Develop.*, vol. 38, no. 2, pp. 161–174, 2001.

[14] S. D. Din, A. Godfrey, C. Mazzà, S. Lord, and L. Rochester, "Free-living monitoring of Parkinson's disease: Lessons from the field," *Movement Disorders*, vol. 31, no. 9, pp. 1293–1313, Sep. 2016.

[15] A. J. Espay *et al.*, "Technology in Parkinson's disease: Challenges and opportunities," *Movement Disorders*, vol. 31, no. 9, pp. 1272–1282, Apr. 2016.

[16] W. Maetzler, J. Klucken, and M. Horne, "A clinical view on the development of technology-based tools in managing Parkinson's disease," *Movement Disorders*, vol. 31, no. 9, pp. 1263–1271, Sep. 2016.

[17] R. de la Fuente-Fernández, M. Schulzer, and A. J. Stoessl, "The placebo effect in neurological disorders," *Lancet Neurol.*, vol. 1, no. 2, pp. 85–91, Jun. 2002.

[18] V. Robles-García *et al.*, "Spatiotemporal gait patterns during overt and covert evaluation in patients with Parkinson's disease and healthy subjects: Is there a Hawthorne effect?" *J. Appl. Biomech.*, vol. 31, no. 3, pp. 189–194, Jun. 2015.

[19] F. Kluge, H. Gaßner, J. Hannink, C. Pasluosta, J. Klucken, and B. M. Eskofier, "Towards mobile gait analysis: Concurrent validity and test-retest reliability of an inertial measurement system for the assessment of spatio-temporal gait parameters," *Sensors*, vol. 17, p. 1522, 2017.

[20] R. Matias, V. Paixão, R. Bouça, and J. J. Ferreira, "A perspective on wearable sensor measurements and data science for Parkinson's disease," *Frontiers Neurol.*, vol. 8, pp. 1–7, Dec. 2017.

[21] H. J. Luinge and P. H. Veltink, "Measuring orientation of human body segments using miniature gyroscopes and accelerometers," *Med. Biol. Eng. Comput.*, vol. 43, no. 2, pp. 273–282, Apr. 2005.

[22] Q. Guo, C. Mastrangelo, and D. J. Young, "Electrical interference suppression technique for 26×26 high-density ground reaction sensor array," in *Proc. IEEE SENSORS*, Dec. 2014, pp. 1220–1223.

[23] P.-H. Chen, R.-L. Wang, D.-J. Liou, and J.-S. Shaw, "Gait disorders in Parkinson's disease: Assessment and management," *Int. J. Gerontol.*, vol. 7, no. 4, pp. 189–193, Dec. 2013.

[24] Z. Chu, P. M. Sarro, and S. Middelhoek, "Silicon three-axial tactile sensor," *Sens. Actuators A, Phys.*, vol. 54, nos. 1–3, pp. 505–510, 1996.

[25] K. Kim *et al.*, "3-axes flexible tactile sensor fabricated by Si micromachining and packaging technology," in *Proc. 19th IEEE Int. Conf. Micro Electro Mech. Syst.*, Jan. 2006, pp. 678–681.

[26] B. J. Kane, M. R. Cutkosky, and G. T. A. Kovacs, "A traction stress sensor array for use in high-resolution robotic tactile imaging," *J. Microelectromech. Syst.*, vol. 9, no. 4, pp. 425–434, Dec. 2000.

[27] M.-Y. Cheng, C.-L. Lin, Y.-T. Lai, and Y.-J. Yang, "A polymer-based capacitive sensing array for normal and shear force measurement," *Sensors*, vol. 10, no. 11, pp. 10211–10225, 2010.

[28] J. Engel, J. Chen, and C. Liu, "Development of polyimide flexible tactile sensor skin," *J. Micromech. Microeng.*, vol. 13, no. 3, p. 359, 2003.

[29] S. Miller and Z. Bao, "Fabrication of flexible pressure sensors with microstructured polydimethylsiloxane dielectrics using the breath figures method," *J. Mater. Res.*, vol. 30, no. 23, pp. 1–11, 2015.

[30] H. K. Lee, J. Chung, S. I. Chang, and E. Yoon, "Normal and shear force measurement using a flexible polymer tactile sensor with embedded multiple capacitors," *J. Microelectromech. Syst.*, vol. 17, no. 4, pp. 934–942, 2008.

[31] H.-K. Lee, S.-I. Chang, and E. Yoon, "A flexible polymer tactile sensor: Fabrication and modular expandability for large area deployment," *Microelectromech. Syst., J.*, vol. 15, no. 6, pp. 1681–1686, Dec. 2006.

[32] B. Li, Y. Shi, H. Hu, A. Fontecchio, and Y. Visell, "Assemblies of microfluidic channels and micropillars facilitate sensitive and compliant tactile sensing," *IEEE Sensors J.*, vol. 16, no. 24, pp. 8908–8915, Dec. 2016.

[33] J. Missinne *et al.*, "Ultra thin optical tactile shear sensor," *Procedia Eng.*, vol. 25, pp. 1393–1396, Jan. 2011.

[34] K. F. Lei, K.-F. Lee, and M.-Y. Lee, "Development of a flexible PDMS capacitive pressure sensor for plantar pressure measurement," *Microelectron. Eng.*, vol. 99, pp. 1–5, Nov. 2012.

[35] P. Yu, W. Liu, C. Gu, X. Cheng, and X. Fu, "Flexible piezoelectric tactile sensor array for dynamic three-axis force measurement," *Sensors*, vol. 16, no. 6, p. 819, Jun. 2016.

[36] A. Charalambides and S. Bergbreiter, "A novel all-elastomer MEMS tactile sensor for high dynamic range shear and normal force sensing," *J. Micromech. Microeng.*, vol. 25, no. 9, Aug. 2015, Art. no. 095009.

[37] H. Cong and T. Pan, "Photopatternable conductive PDMS materials for microfabrication," *Adv. Funct. Mater.*, vol. 18, no. 13, pp. 1912–1921, Jul. 2008.

[38] J. Fernandes and H. Jiang, "Three axis capacitive touch sensor for clinical breast examination training," in *Proc. IEEE SENSORS*, vol. 1, Oct. 2016, pp. 16–18.

[39] J. Vaicekauskaite, P. Mazurek, S. Vudayagiri, and A. L. Skov, "Mapping the mechanical and electrical properties of commercial silicone elastomer formulations for stretchable transducers," *J. Mater. Chem. C*, vol. 8, no. 4, pp. 1273–1279, 2020.

[40] N. Na and L. Zhang, "Dielectric elastomer sensors," in *Elastomers*. London, U.K.: InTech, 2017, pp. 231–253.

[41] S. Eom and S. Lim, "Stretchable complementary split ring resonator (CSRR)-based radio frequency (RF) sensor for strain direction and level detection," *Sensors*, vol. 16, no. 10, p. 1667, Oct. 2016.

[42] E.-S. Hwang, J.-H. Seo, and Y.-J. Kim, "A polymer-based flexible tactile sensor for both normal and shear load detections and its application for robotics," *J. Microelectromech. Syst.*, vol. 16, no. 3, pp. 556–563, Jun. 2007.

[43] H.-K. Lee, J. Chung, S.-I. Chang, and E. Yoon, "Real-time measurement of the three-axis contact force distribution using a flexible capacitive polymer tactile sensor," *J. Micromech. Microeng.*, vol. 21, no. 3, Mar. 2011, Art. no. 035010.

[44] C.-F. Hu, W.-S. Su, and W. Fang, "Development of patterned carbon nanotubes on a 3D polymer substrate for the flexible tactile sensor application," *J. Micromech. Microeng.*, vol. 21, no. 11, Oct. 2011, Art. no. 115012.

[45] S. Pyo *et al.*, "Development of a flexible three-axis tactile sensor based on screen-printed carbon nanotube-polymer composite," *J. Micromech. Microeng.*, vol. 24, no. 7, Oct. 2014, Art. no. 115012.

[46] C. Ma, L.-S. Hsu, J.-C. Kuo, and Y.-J. Yang, "A flexible tactile and shear sensing array fabricated using a novel buckypaper patterning technique," *Sens. Actuators A, Phys.*, vol. 231, pp. 21–27, Jul. 2015.

[47] Y. Liu *et al.*, "A flexible capacitive 3D tactile sensor with cross-shaped capacitor plate pair and composite structure dielectric," *IEEE Sensors J.*, vol. 21, no. 2, pp. 1378–1385, Jan. 2021.

Jayer Fernandes (Student Member, IEEE) received the B.E. degree in electronics and communications engineering from Visvesvaraya Technological University, Karnataka, India, in 2009, and the M.S. degree in electrical and computer engineering from the University of Wisconsin–Madison, Madison, WI, USA in 2014, where he is currently pursuing the Ph.D. degree with the Department of Electrical and Computer Engineering. His research focuses on the development of flexible capacitive and photonic sensors for different biomedical applications. His research interests include implantable optical sensors, micro-optics, and flexible electronics incorporating a wide range of sensing modalities.

Jiangang Chen received the B.E. degree in electronic science and technology from Heilongjiang University, Harbin, Heilongjiang, China, in 2018. He is currently pursuing the Ph.D. degree in electrical and computer engineering with the University of Wisconsin–Madison, Madison, WI, USA. His research interests include pressure/strain sensors, flexible capacitive sensors, optical sensors, and acoustic sensors.
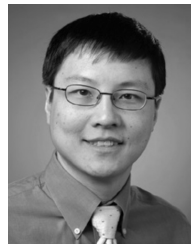
Hongrui Jiang (Fellow, IEEE) received the B.S. degree in physics from Peking University, Beijing, China, and the M.S. and Ph.D. degrees in electrical engineering from Cornell University, Ithaca, NY, USA, in 1999 and 2001, respectively.

From 2001 to 2002, he was a Postdoctoral Researcher with the Berkeley Sensor and Actuator Center, University of California at Berkeley. He is currently the Vilas Distinguished Achievement Professor and the Lynn H. Matthias Professor of engineering with the Department of Electrical and Computer Engineering, a Faculty Affiliate with the Department of Biomedical Engineering, the Department of Materials Science and Engineering, and the Department of Ophthalmology and Visual Sciences, and a member of the McPherson Eye Research Institute with the University of Wisconsin–Madison. His research interests are include microfabrication technology, biological and chemical microsensors, microactuators, optical microelectromechanical systems, smart materials and micro-/nano-structures, lab-on-chip, and biomimetics and bioinspiration. He is a member of the Editorial Board of the IEEE/ASME JOURNAL OF MICROMECHANICAL SYSTEMS. He is a fellow of the Institute of Physics, the Royal Society of Chemistry, the American Institute for Medical and Biological Engineering, and the Institute of Electrical and Electronics Engineers. He was a recipient of the National Science Foundation CAREER Award and the Defense Advanced Research Projects Agency Young Faculty Award in 2008, the H. I. Romnes Faculty Fellowship of the University of Wisconsin–Madison in 2011, the National Institutes of Health Directors New Innovator Award in 2011, the Vilas Associate Award of the University of Wisconsin in 2013, and the Research to Prevent Blindness Stein Innovation Award in 2016.